Journal of Solid State Chemistry 182 (2009) 2579–2586

Contents lists available at ScienceDirect

Journal of Solid State Chemistry

journal homepage: www.elsevier.com/locate/jssc

Effects of Mn substitution on the structure and properties of chalcopyrite-type $CuInSe_2$

Jinlei Yao [a], Carly N. Kline [a], Hao Gu [b], Mi Yan [b], Jennifer A. Aitken [a,*]

[a] Department of Chemistry and Biochemistry, Duquesne University, Pittsburgh, PA 15282, USA
[b] State Key Laboratory of Silicon Materials, Zhejiang University, Hangzhou 310027, China

ARTICLE INFO

Article history:
Received 5 March 2009
Received in revised form
30 June 2009
Accepted 4 July 2009
Available online 15 July 2009

Keywords:
Dilute magnetic semiconductor
Diamond-like semiconductor
Chalcopyrite
Sphalerite
Phase transition
Antiferromagnetic
Photovoltaic
CIS
Solar cell

ABSTRACT

Mn-doped $CuInSe_2$ compounds ($CuIn_{1-x}Mn_xSe_2$, $x = 0.0125–0.20$ and $Cu_{1-y}In_{1-y}Mn_{2y}Se_2$, $2y = 0.0125–0.60$) were synthesized by high-temperature solid-state reactions. Single phase materials with chalcopyrite structure persist up to 0.10 and 0.20 doping for $CuIn_{1-x}Mn_xSe_2$ and $Cu_{1-y}In_{1-y}Mn_{2y}Se_2$, respectively. The chalcopyrite and sphalerite phases co-exist in the $Cu_{1-y}In_{1-y}Mn_{2y}Se_2$ system for $2y = 0.25–0.50$. Attempts to introduce greater manganese content, $x = 0.15–0.20$ for $CuIn_{1-x}Mn_xSe_2$ and $2y = 0.60$ for $Cu_{1-y}In_{1-y}Mn_{2y}Se_2$, result in partial phase segregation. For the single-phase samples, the lattice parameters of both systems increase linearly with manganese concentration and thus follow Vegard's law. The temperature of the chalcopyrite–sphalerite phase transition is decreased by manganese substitution for all single-phase samples. The bandgap of the materials remains around 0.9 eV. Additionally, the Mn-doped $CuInSe_2$ compounds display paramagnetic behavior, whereas pure $CuInSe_2$ is diamagnetic at 5–300 K. All the $CuIn_{1-x}Mn_xSe_2$ and $Cu_{1-y}In_{1-y}Mn_{2y}Se_2$ compounds with chalcopyrite structure show antiferromagnetic coupling and measured effective magnetic moments up to 5.8 μ_B/Mn.

1. Introduction

Copper indium diselenide, $CuInSe_2$, has been intensively investigated for use in next-generation solar cells [1]. Its energy conversion efficiency has been improved by alloying. For instance, impressive progress has been achieved on $Cu(In,Ga)Se_2$-based solar cells, whose efficiency is as high as 19.3% [2]. However, the high cost and low availability of indium and gallium are currently obstacles to the widescale production of $CuInSe_2$-based solar cells. Thus some researchers have considered binary–ternary solid solutions in the corresponding sulfide system, such as $ZnS–CuInS_2$ [3], to incorporate a considerable fraction of low-cost elements. Here we consider the direct replacement of indium by manganese.

In addition to its photovoltaic properties, $CuInSe_2$, as well as other chalcopyrite-type compounds, have been considered as parent materials for dilute magnetic semiconductors (DMSs) [4–6]. Previous research in the area of DMSs has focused on sphalerite-type II–VI and III–V systems doped with manganese [7]. II–VI DMS materials have been found to be mostly antiferromagnetic (AFM) or spin glass [8]. Ferromagnetism (FM) has been observed in the Mn-doped III–V systems, such as $Ga_{1-x}Mn_xAs$ [9]. It is generally accepted that the ferromagnetic behavior originates from the coupling of magnetic ions with holes, and hence the Curie temperature (T_C) is proportional to the density of the magnetic ions and holes. Therefore, in order to push the T_C to room temperature or above, one must be able to incorporate a significant amount of the magnetic ions into the crystal structure of the semiconductor matrix. However, in the case of GaAs:Mn, the manganese solid solubility can only reach 7 at% while maintaining phase purity, and thus the highest T_C is no higher than 110 K [9]. Recently, reports of intriguing room-temperature FM in several Mn-doped II–IV–V_2 chalcopyrites, e.g., $Cd_{1-x}Mn_xGeP_2$ [10] and $Zn_{1-x}Mn_xGeP_2$ [11], have appeared in the literature; however, the validity of these reports is questionable [12]. Chalcopyrites (space group *I*-42*d*) are the ternary analogues of sphalerite binaries by doubling the unit cell along the four-fold axis (Fig. 1). Since there are two cation sites in the chalcopyrite-type semiconductors, the magnetic ions could be easily and selectively substituted in these two sites and thus the resulting magnetic and magnetotransport properties can be tuned due to the compositional flexibility of site substitution.

$CuInSe_2$-based compounds can be prepared both n- and p-type depending on synthetic conditions, which is in favor of the fabrication of p–n homojunctions. Very recently, Matsushita et al. [13] also studied the Mn-substituted $CuInSe_2$ solid solutions and found the manganese solubility limitation reached up to 10% in

* Corresponding author. Fax: +1 412 396 5683.
E-mail address: aitkenj@duq.edu (J.A. Aitken).

0022-4596/$ - see front matter © 2009 Elsevier Inc. All rights reserved.
doi:10.1016/j.jssc.2009.07.014

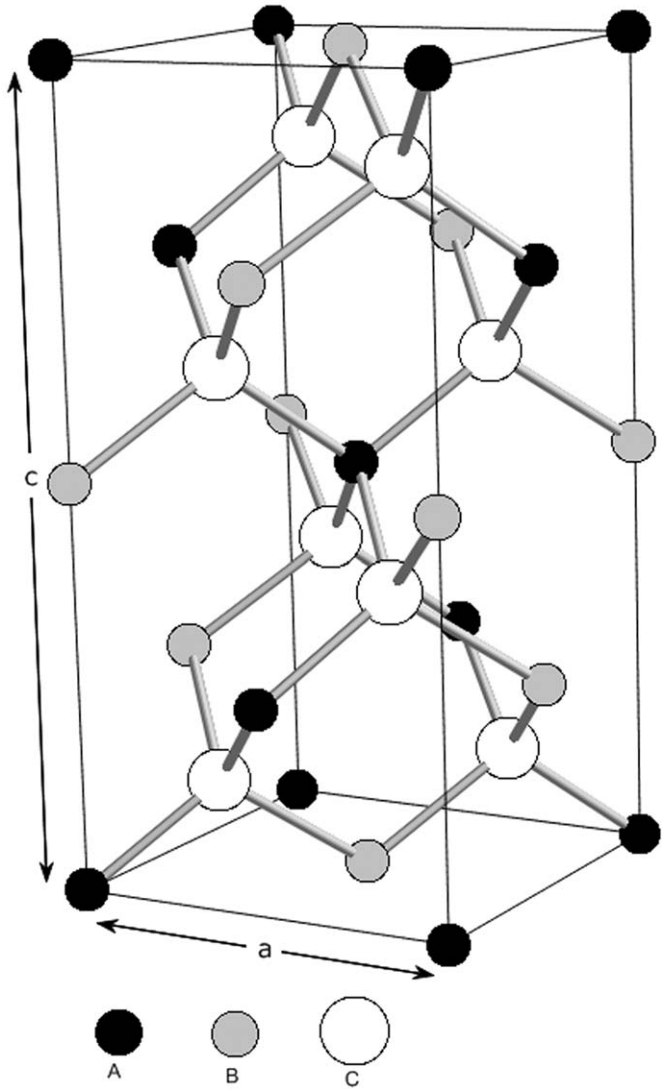

Fig. 1. The chalcopyrite crystal structure, ABC_2 (A on 4*a* (0,0,0), B on 4*b* (0,0,0.5) and C on 8*d* (*x*,0.25,0.125) with *x* close to 0.25).

the Cu or In sites. However, a detailed study of the effects of Mn doping on the crystal structure and magnetic properties have not been reported. We herein report the effects of manganese substitution on chemical composition, crystal structure, optical and magnetic properties. As high as 20% Mn can be incorporated in $CuInSe_2$, while maintaining phase-pure samples that crystallize in the chalcopyrite-type structure. Interestingly, in the case of doping on both cation sites a disordered sphalerite phase coexists with the chalcopyrite phase up to 50% Mn.

2. Experimental

2.1. Reagents

The chemicals in this work were used as obtained unless otherwise noted: (i) copper powder, −100 mesh, 99.999%, Strem; (ii) indium powder, −325 mesh, 99.99%, Strem; (iii) manganese chips, 0.8–3 mm, 99.99%, Cerac; (iv) selenium powder, −200 mesh, 99.99%, Strem. The manganese pieces were cleaned with hot 10% HNO_3 in methanol and then ground into powder in an argon-filled glovebox.

2.2. Synthesis

The powder samples with a nominal composition $CuIn_{1-x}Mn_xSe_2$ ($x = 0.0125$–0.20) and $Cu_{1-y}In_{1-y}Mn_{2y}Se_2$ ($2y = 0.0125$–0.60) were synthesized by high-temperature, solid-state reactions of the elements using a modified literature procedure [14]. Additionally, an undoped sample was also prepared for comparison purposes. As an example, 8 mmol of $CuIn_{1-x}Mn_xSe_2$ ($x = 0.05$) was prepared by grinding 0.5084 g of Cu powder, 0.8726 g of In powder, 0.0220 g of Mn powder and 1.2634 g of Se powder for 10 min and loading the mixture into a 9 mm o.d. fused-silica tube in an Ar-filled glovebox. The fused-silica tube was sealed under a vacuum of approximately 10^{-3} mbar using a natural gas/oxygen torch, and then placed into a programmable furnace. The samples were heated from room temperature to 1000 °C in 12 h and maintained at 1000 °C for 72 h, before being cooled to room temperature in 12 h. After cooling, the samples were removed from the tubes, inspected under an optical microscope, and ground for characterization.

2.3. Physical measurements

2.3.1. Powder X-ray diffraction (PXRD) and Rietveld refinement

PXRD patterns were collected using a PANalytical X'pert PRO MPD powder X-ray diffractometer with the X'celerator detector, 1/4° divergence slit, 1/2° anti-scatter slit, 0.02 rad soller silt at both incident and diffracted beams, operating at 45 kV and 40 mA in the Bragg–Brentano geometry and using Cu*K*α radiation. Scans were performed from 15° to 145° 2θ with a step width of 0.008° and a scan speed of 0.010644°/s. Samples were prepared for analysis by grinding the sample powder for over half an hour in an agate mortar and pestle and then back filling the powder into the aluminum sample holder. Silicon powder from the Gem Dugout was used as an internal standard reference to correct the sample height displacement and the zero point [15]. Crystalline phases were identified using the search match capabilities of the X'pert HighScore Plus [16] program along with the International Centre for Diffraction Data (ICDD) powder diffraction file (PDF) database.

The Rietveld refinements were carried out using GSAS with an interface of EXPGUI [17,18]. A Pseudo-Voigt function with the Finger–Cox–Jephcoat asymmetry correction was used to model the peak profile and the background was described as a shifted Chebyschev type. The following parameters were refined: scale factor, background parameters, lattice parameters, peak shape parameters, sample displacement, atomic coordinates, isotropic displacement parameters (U_{iso}) and site occupation factors (SOFs).

2.3.2. Scanning electron microscopy (SEM)/energy dispersive X-ray spectroscopy (EDS)

Samples were mounted onto double-sided carbon tape which was adhered to an aluminum specimen holder. A CamScan Series 4 SEM was employed to image samples and a Princeton Gamma Tech detector was used for EDS. The working distance was 35 mm and the accelerating voltage was set to 22.5 kV. EDS spectra were collected with an accumulation time of 60 s. To determine the elemental distribution in the samples, X-ray maps were recorded for over 30 min.

2.3.3. Inductively coupled plasma (ICP)

Quantitative analysis of Cu, In, Mn and Se was performed by RJ Lee Group, Inc. (Monroeville, PA), using inductively coupled plasma optical emission spectrometry (ICP-OES) and inductively coupled plasma mass spectrometry (ICP-MS). Sample were digested with trace metal nitric acid (Fisher Scientific) using the

high pressure XP1500 vessels in a MarsExpress CEM Microwave system. Samples were held at 180 °C for 20 min. The digested samples were analyzed in a Varian 730ES ICP-OES for Cu, In and Mn, and in a Perkin Elmer ELAN 9000 ICP-MS for Se.

2.3.4. Differential thermal analysis (DTA)

DTA was performed using a Shimadzu DTA-50 thermal analyzer. DTA data were recorded using the TA60-WS collection program. The instrument was calibrated with a three-point calibration curve using the melting points of indium, zinc and gold metals. The temperature was programmed to increase at a rate of 10 °C/min from 25 to 1100 °C, and then to decrease to 100 °C at 10 °C/min. To determine the reversibility of the events, a second cycle was performed in the same manner. The reference, Al_2O_3, obtained from Shimadzu Corporation, and sample were contained in fused-silica ampoules and sealed under a vacuum of $\sim 10^{-3}$ mbar. The melting point was determined from the peak of the endothermic event.

2.3.5. Optical spectroscopy

Optical diffuse reflectance spectra were measured on a Cary 5000 UV–Vis–NIR spectrophotometer, equipped with the Harrick praying mantis diffuse reflectance accessory, from 2500 to 200 nm at a scanning rate of 600 nm/min. $BaSO_4$ powder (Fisher, 99.92%) was used as a 100% reflectance standard. The absorbance–energy curve was used to estimate the bandgap (E_g) by converting reflectance to absorption data using the Kubelka–Munk equation [19]. E_g is determined by the extrapolation of the absorption edge to the baseline.

2.3.6. Magnetic measurements

DC magnetization studies were carried out using a superconducting quantum interference device magnetometer (Quantum Design MPMS-7). The temperature dependence of magnetization data were measured from 5 to 300 K under an applied field of 5 kOe under zero-field-cooling conditions. Approximately 30 mg of powder were packed in a capsule for magnetic measurements, and the magnetic susceptibility of the Mn-doped samples were corrected for the diamagnetic contribution from the capsule and the undoped $CuInSe_2$ sample.

3. Results and discussion

3.1. Synthesis and SEM/EDS

The polycrystalline $CuIn_{1-x}Mn_xSe_2$ ($x = 0.0125$–0.20) and $Cu_{1-y}In_{1-y}Mn_{2y}Se_2$ ($2y = 0.0125$–0.60) ingots synthesized via high-temperature solid-state reactions are grayish black. The EDS analysis suggests that the measured compositions of the compounds are close to the intended stoichiometries. For instance, the EDS analysis on $CuIn_{1-x}Mn_xSe_2$ ($x = 0.05$) shows the constituent elemental ratio of Cu:In:Mn:Se = 0.93:0.89:0.05:2.13. The X-ray maps obtained for selected samples, $CuIn_{1-x}Mn_xSe_2$ ($x = 0.05$) and $Cu_{1-y}In_{1-y}Mn_{2y}Se_2$ ($2y = 0.05$ and 0.10), suggest that all elements, copper, indium, selenium and manganese, distribute homogenously in the samples (Fig. 2 and Fig. S1 in supplementary material).

3.2. Chemical composition by ICP

Since the EDS analysis is only semi-quantitative, the chemical composition of the samples was determined quantitatively by ICP-OES and ICP-MS, see Table 1. ICP data show that the ratio of Mn/In is quite close to the intended stoichiometry, and the measured Se composition is slightly lower than the nominal composition. This suggests that the samples may be slightly Se-poor, or the selenium content may be low due to H_2Se loss during sample digestion.

3.3. Structural characterization and phase transition

3.3.1. Phase identification and thermal analysis

The PXRD patterns (Fig. 3) reveal that $CuIn_{1-x}Mn_xSe_2$ forms single-phase compounds, crystallizing in the chalcopyrite-type structure up to $x = 0.10$, in agreement with the results of Ref. [13]. However, the lattice-parameter dependence on manganese concentration was not reported in that work [13]. As the manganese concentration is increased, partial phase segregation is apparent, as a few weak peaks in the PXRD patterns of $x = 0.15$ and 0.20 samples can be indexed to CuSe [20] and $MnSe_2$ [21], respectively, although the majority of the peaks can still be attributed to the tetragonal chalcopyrite phase. The DTA profiles (Fig. S2 and Table S1) of $CuIn_{1-x}Mn_xSe_2$ compounds show that the melting point remains constant (~983 °C) whereas the

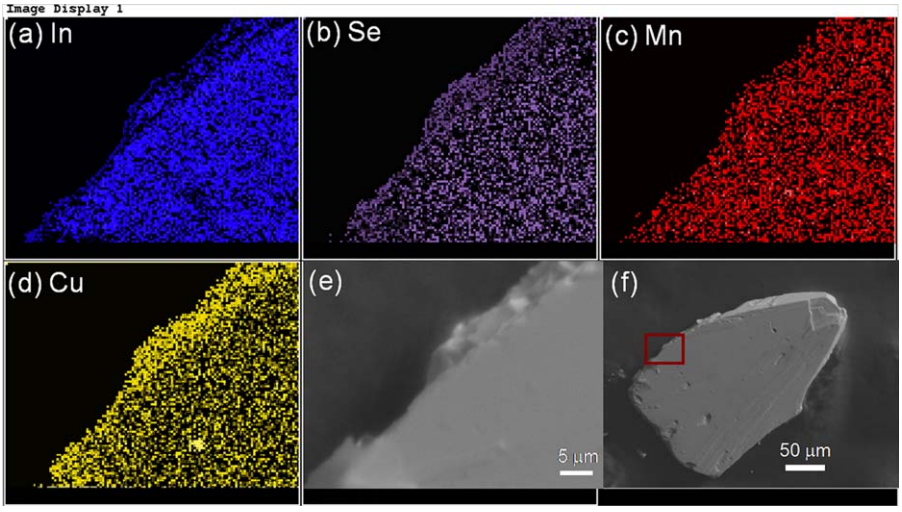

Fig. 2. Elemental maps of (a) In, (b) Se, (c) Mn and (d) Cu, and (e, f) SEM images of $CuIn_{1-x}Mn_xSe_2$ ($x = 0.05$), where (e) is the enlarged image of the rectangular box in (f).

Table 1
Chemical composition of $CuIn_{1-x}Mn_xSe_2$ compounds measured by ICP.

x	Cu	In	Mn	Se
0	0.98(5)	1.00(5)	0	1.90(10)
0.0125	1.06(5)	0.987(5)	0.013(1)	1.84(10)
0.025	1.08(5)	0.968(5)	0.032(2)	1.95(10)
0.05	0.98(5)	0.951(5)	0.049(2)	1.94(10)
0.10	1.04(5)	0.888(4)	0.112(6)	1.91(10)

The sum of In and Mn is normalized.

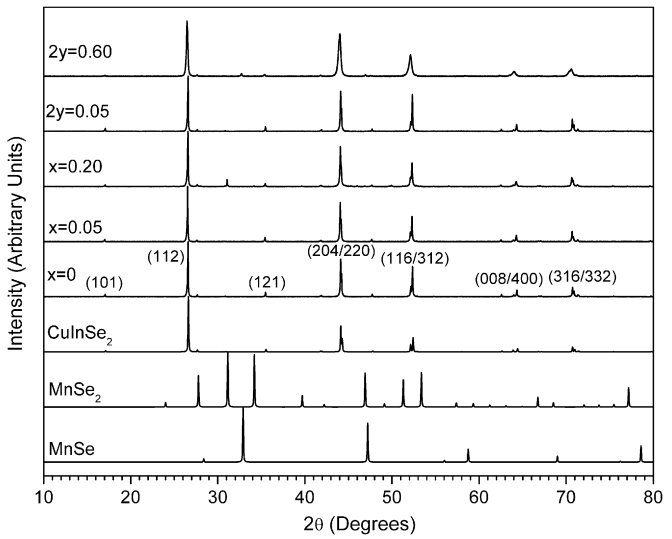

Fig. 3. Powder X-ray diffraction patterns for $CuIn_{1-x}Mn_xSe_2$ and $Cu_{1-y}In_{1-y}Mn_{2y}Se_2$ compounds, compared with reference patterns ($CuInSe_2$: JCPDS # 01–081–1936, $MnSe_2$: JCPDS # 01–073–1525 and MnSe: JCPDS # 03–065–6528). (*hkl*) denotes the Miller indices of chalcopyrite-type structure. Several indexed peaks of low intensity are unlabeled on the figure for clarity purposes, however, they were used for Rietveld refinements.

chalcopyrite–sphalerite (T_{C-S}) phase transition is driven to lower temperature by the manganese substitution, i.e., from $T_{C-S} = 801\,^{\circ}C$ for $x = 0$ to $T_{C-S} = 747\,^{\circ}C$ for $x = 0.05$, indicating the incorporation of Mn in the crystal structure of the chalcopyrite phase. Two batches of doped samples were prepared and analysis yielded the same results.

The phase identification of the $Cu_{1-y}In_{1-y}Mn_{2y}Se_2$ system shows that the presence of unwanted phases does not appear until $2y = 0.60$ (Fig. 3). In this case, the extra peaks can be indexed to MnSe [22]. At first glance, it seems that the single-phase chalcopyrite can survive up to the manganese doping of 50% on both Cu and In sites. However, one can see that some of the chalcopyrite-type peaks (*hkl* = 112, 204/220, 116/312, 008/400, 316/332) are greatly broadened when the manganese content is ≥ 0.25 in $Cu_{1-y}In_{1-y}Mn_{2y}Se_2$ (Fig. 3). Often times, peak broadening can be attributed to small-size grains or poor crystallinity of the sample. However, other peaks (*hkl* = 101, 103, 121, 301) have relatively sharp profiles and small values of full width at half maximum, excluding both possibilities for our samples. Another explanation can be related to the presence of a secondary phase similar to the chalcopyrite phase. Interestingly, these broadened peaks can be indexed to those of the sphalerite-type phase (space group $F\bar{4}3m$) where the Cu, In and Mn would occupy the same cation site, i.e., (*hkl*) = (111, 220, 311, 400, 331). Fig. 4 shows the PXRD patterns of $2y = 0$–0.50 around the (112) and (204/220) peaks in detail. One can see that the peak positions are shifted to lower angles from $2y = 0$ to 0.50 which indicates lattice expansion due to the manganese substitution, and a shoulder appears at the

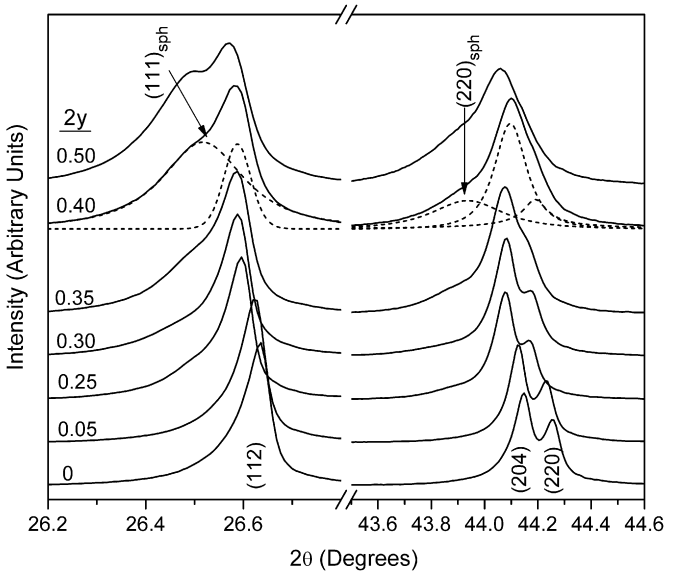

Fig. 4. Powder X-ray diffraction patterns for $Cu_{1-y}In_{1-y}Mn_{2y}Se_2$ compounds. (*hkl*) and $(hkl)_{sph}$ denote the Miller indices of chalcopyrite- and sphalerite-type structures, respectively. For the sample with $2y = 0.40$, the peaks are fitted by a Pearson-VII function.

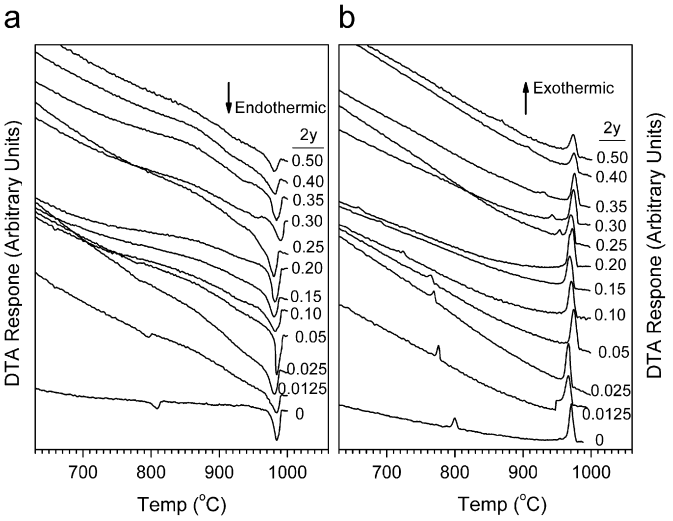

Fig. 5. Differential thermal analysis diagrams for $Cu_{1-y}In_{1-y}Mn_{2y}Se_2$ compounds. The heating and cooling cycles are shown in (a) and (b), respectively.

lower-angle sides of the peaks. For $2y = 0.25$–0.50, the patterns can be well fit by a Pearson-VII function with the characteristic peaks of chalcopyrite and sphalerite phases. The DTA profiles of $Cu_{1-y}In_{1-y}Mn_{2y}Se_2$ system show that the chalcopyrite–sphalerite phase transition is driven to lower temperature by the introduction of greater amounts of manganese, i.e., from $T_{C-S} = 776\,^{\circ}C$ for $2y = 0.0125$ to $T_{C-S} = 659\,^{\circ}C$ for $2y = 0.20$, indicating the incorporation of Mn in the crystal structure of the chalcopyrite phase (Fig. 5 and Table S2). It is noteworthy that the DTA profile of $2y = 0.25$ displays a phase transition at 970 °C near the melting point upon cooling (Fig. 5b), and this phase transition can also be observed in the other samples with $2y > 0.25$. Since the $Cu_{1-y}In_{1-y}Mn_{2y}Se_2$ ($2y = 0.25$–0.50) compounds are a mixture of chalcopyrite and sphalerite-type phases at room temperature as analyzed by PXRD, this transition can be considered as a partial sphalerite–chalcopyrite phase transition upon cooling with some residual sphalerite-type phase persisting down to room

temperature. A similar two-phase coexistence and phase transition have been also observed in the solid solutions of ZnS–$CuInS_2$ [3] and CdSe–$CuInSe_2$ [23].

3.3.2. Rietveld refinement

3.3.2.1. $CuIn_{1-x}Mn_xSe_2$ system. In order to study the manganese-doping effect on crystal structure in detail, the Rietveld refinement of laboratory PXRD data obtained for the $CuIn_{1-x}Mn_xSe_2$ ($x = 0$–0.20) system was carried out (Fig. 6 and Fig. S3). In the chalcopyrite structure, there are two cation sites, 4*a* (0,0,0) and 4*b* (0,0,0.5), and one anion on 8*d* (*x*, 0.25, 0.125) with *x* close to 0.25. It can be viewed as a cubic closest packing of anions with cations residing in half of the tetrahedral holes. In most chalcopyrites a small tetragonal distortion presents when the ratio between the lattice parameters, *a* and *c* ($\eta = c/2a$), deviates from 1. Moreover its anion is slightly displaced from the ideal sphalerite site. For instance, in $CuInSe_2$, each Se anion has two Cu and two In cations as its nearest neighbors with Cu closer than In. For a complete determination of the crystal structure, only three parameters are required besides the atomic displacement parameters: the unit cell parameters, *a* and *c*, and the anion coordinate, *x*. In our Rietveld refinements of the $CuIn_{1-x}Mn_xSe_2$ system, the tetragonal distortion η, ~1.0050, is found to be nearly identical to that of $CuInSe_2$ crystals reported in literature (Table S3). The selenium coordinate, x_{se}, is determined to be ~0.23 (Table 2), within the reported range of 0.223–0.235 found in literature [24–28].

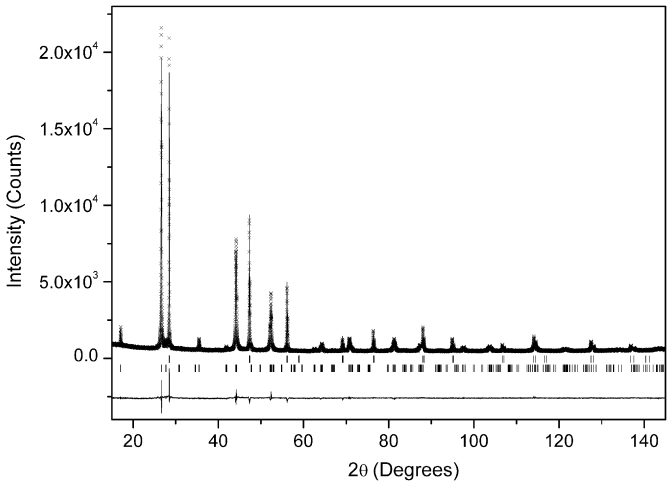

Fig. 6. Rietveld refinement of $CuIn_{1-x}Mn_xSe_2$ ($x = 0.10$, $wR_p = 5.67\%$, $R_p = 4.32\%$, $\chi^2 = 2.171$). Observed (+++) and calculated (solid line) X-ray diffraction patterns are shown on top. The difference between observed and calculated intensities is shown as a difference plot on the bottom. Two sets of tick marks between the X-ray and difference patterns indicate the Bragg reflections of Si and Cu(In,Mn)Se_2 from top to bottom, respectively.

The cell parameters determined from the Rietveld refinement of $CuIn_{1-x}Mn_xSe_2$ are exhibited in Fig. 7 and Table S3. The cell parameters, *a* and *c*, of $x = 0$ are determined to be 5.7842(1) and 11.6266(3) Å, respectively, which are in good agreement with the reported values of $a = 5.780$–5.7877 Å and $c = 11.609$–11.6464 Å for powder or single crystal $CuInSe_2$ samples [24–28]. The lattice parameters are found to increase linearly with increasing manganese concentration in the single-phase $CuIn_{1-x}Mn_xSe_2$ ($x = 0$–0.10) compounds (Fig. 7) as expected, due to the slightly larger ionic radius of manganese compared to that of indium ($r^{2+}_{Mn} = 0.80$ Å and $r^{3+}_{In} = 0.76$ Å) [29]. The linear dependence of lattice parameters upon the manganese content follows Vegard's law [30], suggesting a random distribution of manganese ions on the indium site. Although the samples of $x = 0.15$–0.20 show some minor phase separation, the lattice parameters of the major chalcopyrite-type phase still increase. However, they deviate from the linear relationship and were not used to fit the line shown in Fig. 7. The Rietveld refinement of $CuIn_{1-x}Mn_xSe_2$ with $x = 0.15$ reveals the coexistence of two phases, namely, 95.1 wt% chalcopyrite phase and 4.9 wt% CuSe (Fig. S3).

To elucidate the effect of Mn doping on the chemical composition, we refined the SOFs using the Rietveld method. In the refinement of the undoped sample, the refined SOFs suggest that the sample is Se-poor (SOF(In) fixed at 1, SOF(Cu) = 0.995(6) and SOF(Se) = 0.972(9)). The isotropic displacement parameters are found to be considerably larger for Cu atoms ($U_{iso} = 0.0213(19)$ Å^2) than those for In ($U_{iso} = 0.0076(9)$ Å^2) and Se ($U_{iso} = 0.0180(13)$ Å^2). These results indicate the same tendency as that found in the single crystal and polycrystalline studies carried out by others [24,26,28]. In order to compare the doping effect on SOF, U_{iso} of Se was fixed to be identical, 0.01803 Å^2, for the whole series of samples and the total SOF of the cation 4*b* site is constrained at unity. The refined results are gathered in Table 2. It can be seen that all of the samples are Se-poor, in agreement with the results of ICP. The refined Mn composition is very close to the nominal one, however, the samples are determined to be Cu-deficient as $x \geq 0.025$. It should be noted that the occupation of Mn on the 4*b* site is only one

Table 2
Structural parameters obtained from Rietveld refinement of powder X-ray diffraction data for $CuIn_{1-x}Mn_xSe_2$ compounds.

Parameters	Nominal composition of $CuIn_{1-x}Mn_xSe_2$				
	$x = 0$	$x = 0.0125$	$x = 0.025$	$x = 0.05$	$x = 0.10$
Cation 4a					
SOF(Cu)	0.995(6)	1.009(6)	0.962(7)	0.977(6)	0.961(7)
$100U_{iso}$ (Å^2)	2.134(186)	1.858(170)	1.267(161)	2.261(177)	1.781(186)
Cation 4b					
SOF(In/Mn)	1/0	0.987(6)/0.013(6)	0.975(7)/0.025(7)	0.949(6)/0.051(6)	0.900(7)/0.100(7)
$100U_{iso}$ (Å^2)	0.760(85)	1.056(64)	1.111(64)	1.354(64)	1.403(73)
Anion8d					
SOF(Se)	0.972(9)	0.985(4)	0.993(5)	0.949(4)	0.971(5)
$100U_{iso}$ (Å^2)	1.803(129)	1.803	1.803	1.803	1.803
x_{Se}	0.2319(5)	0.2299(5)	0.2323(5)	0.2315(5)	0.2312(5)
Reliability factors					
χ^2	2.091	1.949	1.903	2.382	2.171
wR_p	0.0559	0.0539	0.0553	0.0595	0.0567
R_p	0.0430	0.0414	0.0426	0.0452	0.0432

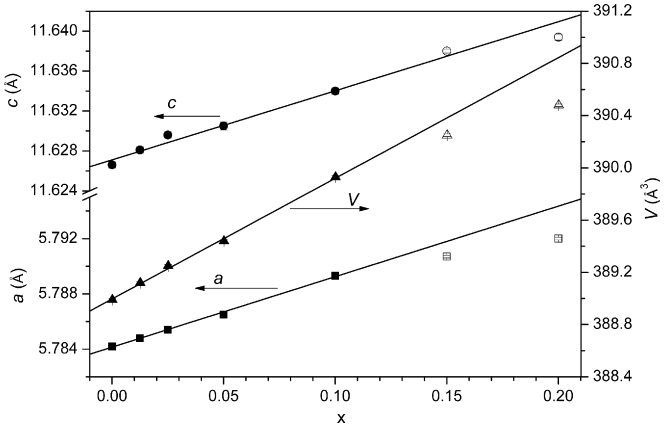

Fig. 7. Manganese concentration versus lattice parameters and volume for $CuIn_{1-x}Mn_xSe_2$ compounds. The lines are the linear fit to the experimental data of $x = 0$–0.10 (solid symbols); the data of $x = 0.15$–0.20 (open symbols) were not used for the linear fit.

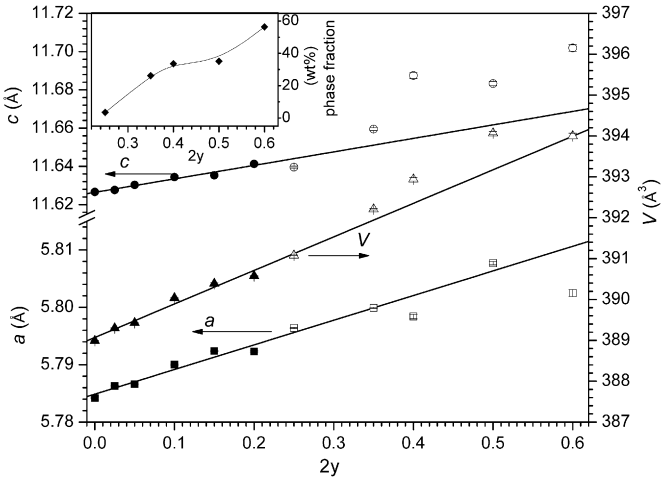

Fig. 8. Manganese concentration versus lattice parameters and volume for $Cu_{1-y}In_{1-y}Mn_{2y}Se_2$ compounds. The lines are the linear fit to the experimental data of $2y = 0$–0.20 (solid symbols); the data of $2y = 0.25$–0.60 (open symbols) were not used for the linear fit. The inset shows the sphalerite-phase fraction as a function of manganese concentration.

plausible model for this system, but it is the best one based on our data. It is also supported by the prediction of preferential occupation of Mn on the 4*b* site by the first-principles calculations in the Cu-rich and III-poor Cu-III–VI_2 chalcopyrites and the analysis of X-ray absorption fine structure measurements on $(MnS)_{2x}(CuInS_2)_{1-x}$ [31,32]. However, we cannot exclude the possibility of Mn ions, at least partially, occupying the 4*a* site because of the notable copper vacancy (~4 at%), even though attempts to refine Mn and Cu on the 4*a* site lead to divergence due to their electronic similarity.

At this point, one might take notice of the charge balance in this system. We will assume that indium is in the 3+ oxidation state. Additionally, we will assume that copper is 1+ since copper ions are almost always Cu^+ in chalcopyrites [33,34], therefore the likelihood of stabilizing Cu^{2+} is a weak possibility. The oxidation state of selenium will be considered as 2−. The manganese oxidation state is more questionable, as it is possible to be 2+ or 3+ in a selenide environment. If the compounds are stoichiometric, the formula would not charge balance with Mn^{2+}, for example $Cu^{+1}In^{3+}_{0.95}Mn^{2+}_{0.05}\ Se^{2-}_2$ (+3.95/−4.0). However, both ICP and Rietveld refinements are suggestive of non-stoichiometric samples.

If we look at the ICP data, for example that obtained for the nominal composition of $CuIn_{1-x}Mn_xSe_2$ with $x = 0.05$, we can calculate +3.93 for the total cation charge assuming only Mn^{2+} and −3.88 total charge from the selenium anions. If we were to consider any amount of Mn^{3+} in the material, the charges would be further from balanced. The same calculation can be performed using the SOFs obtained from Rietveld refinement of the same sample. In this case we obtain +3.926 and −3.796. These data strongly suggest that Mn^{3+} should not be present in the materials, however, one cannot completely rule out the presence of a very small amount of Mn^{3+}, due to the many assumptions made above. Also the presence of Mn^{2+} in the sample was confirmed using preliminary electron paramagnetic resonance (EPR) data.

Neutron diffraction would be a more suitable tool to study these samples, since the difference in the neutron scattering length of these cations is sizable ($b_{Cu} = 7.718$ fm, $b_{Mn} = -3.750$ fm and $b_{In} = 4.065$ fm) [35]. Additionally, there are other intricate possibilities that can arise in the structure of these types of materials that have been documented in the literature. For example, Cu deficiency can arise from the existence of interstitial Cu in the material [28]. Furthermore, the presence of cation antisite defects (In_{Cu} and Cu_{In}) is well known in these systems and has been observed in $CuInSe_2$ crystals using synchrotron X-ray diffraction [28].

3.3.2.2. $Cu_{1-y}In_{1-y}Mn_{2y}Se_2$ system. For the $Cu_{1-y}In_{1-y}Mn_{2y}Se_2$ system, the above phase identification gives evidence of two-phase coexistence, ordered chalcopyrite and disordered sphalerite phases, with high Mn content. Rietveld refinement is a suitable way to perform quantitative phase analysis on this series of compounds. The refinement results are illustrated in Fig. S4 and Table S4. In the single-phase range ($2y = 0$–0.20), the relationship between the lattice parameters and manganese concentration also obeys Vegard's law (Fig. 8). When the manganese ion is further introduced ($2y = 0.25$–0.50), the system enters into a two-phase region. The sphalerite-phase fraction increases from 3.5 wt% for $2y = 0.25$ to 35.1 wt% for $2y = 0.50$ (see the inset of Fig. 8). In the two-phase region, it is reasonable to speculate that the manganese ions occupy one of the cation sites preferentially and thus create Cu–In anti-site occupancy, leading to the chalcopyrite–sphalerite transformation. The same structural transition has been observed due to the cation anti-site occupancy in the ZnX–$CuInX_2$ (X = S, Se, Te) system [3]. The introduction of greater manganese content ($2y = 0.60$) results in the appearance of a third phase, MnSe. Rietveld refinement shows that this sample with $2y = 0.60$ consists of 39.8 wt% chalcopyrite phase, 56.4 wt% sphalerite phase and 3.8 wt% MnSe.

3.4. Optical spectroscopy

Optical diffuse reflectance measurements in the UV/Vis/NIR region were performed on powder samples of $CuIn_{1-x}Mn_xSe_2$ ($x = 0.0125$–0.20) and $Cu_{1-y}In_{1-y}Mn_{2y}Se_2$ ($2y = 0.0125$–0.50) (Fig. 9). Analysis of the spectrum shows an optical absorption edge for the phase-pure, undoped $CuInSe_2$ of approximately 0.92 eV, consistent with the black color of the material and in reasonable agreement with $E_g = 0.98$–1.04 eV found in the literature [36,37]. Analysis of the spectra of the doped samples shows that manganese substitution has little to no effect on the bandgap energy (0.86–0.92 eV). The bandgap variation ($\Delta E_g = 0.06$ eV) with the manganese doping is within the range of the bandgap difference for $CuInSe_2$ reported in the literature [36,37].

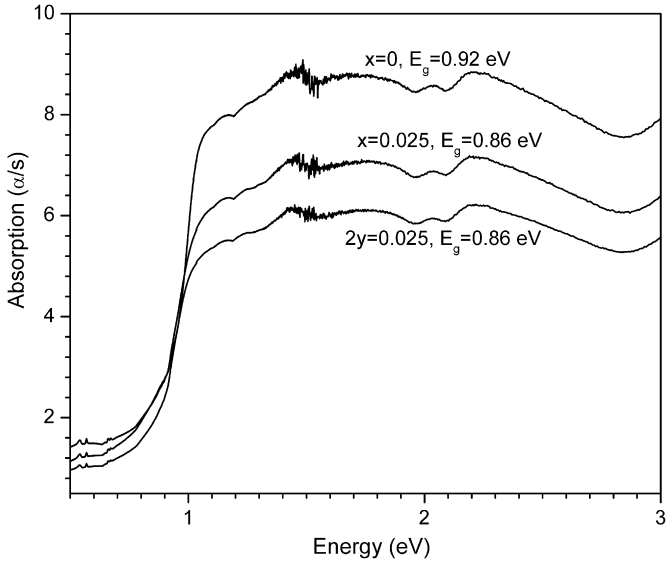

Fig. 9. Diffuse reflectance spectra converted to absorption for $CuIn_{1-x}Mn_xSe_2$ and $Cu_{1-y}In_{1-y}Mn_{2y}Se_2$ compounds. For clarity, only the spectra of the undoped and doped compounds with manganese content of 0.025 are shown.

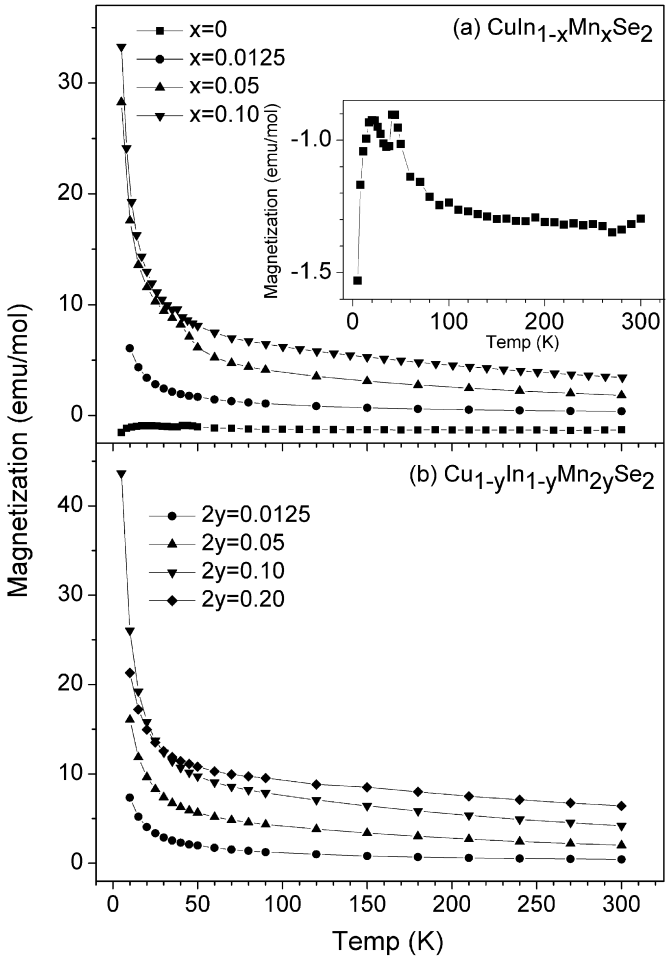

Fig. 10. Temperature dependence of the magnetization for (a) $CuIn_{1-x}Mn_xSe_2$ and (b) $Cu_{1-y}In_{1-y}Mn_{2y}Se_2$ compounds in a magnetic field of 5 kOe. The inset displays the magnetization of undoped $CuInSe_2$ in detail.

3.5. Magnetic properties

In order to understand the manganese-doping effects on magnetic properties, the temperature dependence of the magnetization (M) of Mn-doped, phase-pure, chalcopyrite-type $CuInSe_2$ compounds has been measured in an applied field (H) of 5 kOe (Fig. 10). The pure $CuInSe_2$ compound has a constant diamagnetic magnetization of ~ 1.3 emu/mol as shown in the inset of Fig. 10. Below 50 K there is a paramagnetic tail, which may originate from the magnetic coupling between bound or trapped charge carriers in the sample [38]. This tail has also been observed throughout the doped samples in the same temperature range ($T<50$ K). When the manganese ion is introduced into $CuInSe_2$, the magnetization is inversed from a negative signal to positive one, indicating paramagnetic behavior in the doped samples. There is no indication of a magnetic transition down to 5 K (Fig. 10).

In Fig. 11, the temperature dependence of the inverse magnetic susceptibility, $1/\chi = H/M$, is presented. The molar susceptibility χ above 50 K obeys the Curie–Weiss law. The values of Weiss temperature (θ) are derived using the Curie–Weiss law and listed in Table 3. All the θ values are negative and the absolute magnitude increases with increasing Mn concentration. This suggests that the magnetic interaction between Mn ions is AFM in the Mn-doped $CuInSe_2$ materials and the AFM coupling is enhanced by the Mn concentration. The effective magnetic moments of Mn ions (μ_{eff}) are in the range of 3.9–5.8 μ_B, somewhat smaller than the expected μ_{eff} ($= 5.92\,\mu_B$) of the free Mn^{2+} ion, indicating that the Mn ions may be mixed valent or they

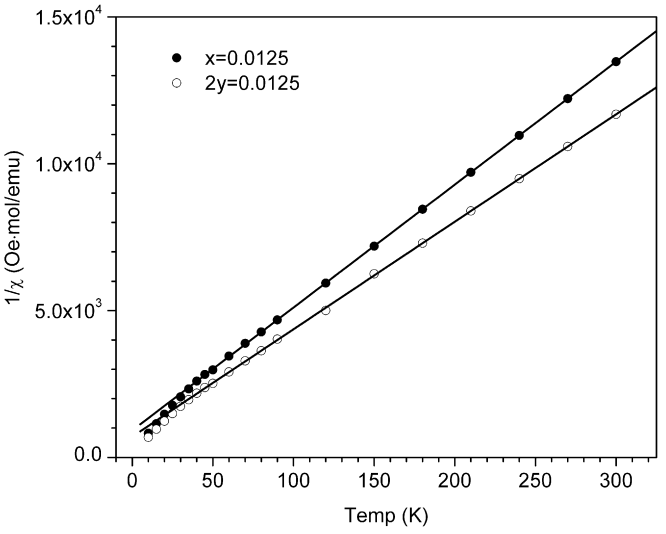

Fig. 11. Temperature dependence of the inverse magnetic susceptibility for $CuIn_{1-x}Mn_xSe_2$ and $Cu_{1-y}In_{1-y}Mn_{2y}Se_2$ compounds. The lines are fit ($T>50$ K) using the Curie–Weiss law. For clarity, only the data of the doped compounds with manganese content of 0.0125 are shown.

Table 3
Weiss temperature, θ, and effective magnetic moment, μ_{eff}, of Mn ions for Mn-doped $CuInSe_2$ compounds.

Mn	0.0125	0.05	0.10	0.20
θ_x (K)	−22	−76	−149	
μ_x (μ_B)	3.9	4.9	5.1	
θ_{2y} (K)	−19	−94	−148	−348
μ_{2y} (μ_B)	4.2	4.9	5.4	5.8

The subscripts, x and $2y$, represent the Mn concentration in the $CuIn_{1-x}Mn_xSe_2$ and $Cu_{1-y}In_{1-y}Mn_{2y}Se_2$ systems, respectively.

form clusters of zero magnetic moment. Since ICP, Rietveld refinement and EPR data suggest the existence of Mn^{2+}, we tend to favor the latter possibility. Both series of doped compounds have similar magnetic behavior, regardless of the dopant sites. This indicates that the short-range AFM coupling between Mn ions, rather than carrier-mediated interactions, may dominate the magnetic properties in these samples. In addition, our preliminary thermopower measurements show that the undoped $CuInSe_2$ and $CuIn_{1-x}Mn_xSe_2$ ($x = 0.05$) samples are p-type.

Although we lack sufficient experimental evidence to give an explicit microscopic picture of the magnetic ordering in Mn-doped $CuInSe_2$, a few empirical pictures of zero-magnetic-moment clusters can be proposed based on our data and the microscopic models of spin correlations in Mn-doped II–VI DMSs and GaAs:Mn [8,39,40]. A plausible picture is one in which the magnetic Mn^{2+}–Mn^{2+} interaction is superexchange AFM coupling mediated through the intervening Se^{2-} anion, leading to the formation of AFM clusters as in Mn-doped II–VI DMSs [8]. The other picture may be related to the presence of Mn interstitial defects, Mn_I. In the case of GaAs:Mn, while most of the Mn ions occupy the gallium site leading to a net ferromagnetic behavior, some Mn ions tend to occupy interstitial sites [39]. Therefore in our materials there could be Mn_I donors, compensating the Mn_{In} and/or Cu_{In} acceptors. The magnetic moments of Mn_I interact antiferromagnetically with the adjacent moments of Mn^{2+} ions on the cation sites, resulting in the formation of zero-magnetic-moment clusters. A similar model of antiferromagnetically ordered Mn_I–Mn_{Ga} pairs was proposed for GaAs:Mn [39,40].

4. Conclusion

In summary, the polycrystalline samples of Mn-doped $CuInSe_2$ have been successfully prepared by high-temperature solid-state reactions. The manganese solid solubility can reach up to 10% and 20% for $CuIn_{1-x}Mn_xSe_2$ and $Cu_{1-y}In_{1-y}Mn_{2y}Se_2$, respectively, while maintaining phase-pure chalcopyrite-type materials. The analysis of ICP and Rietveld refinements reveal that the single-phase $CuIn_{1-x}Mn_xSe_2$ compounds are Se-poor. Neutron diffraction is proposed to further investigate the atomic site occupancy and cation anti-site defects in detail [41]. Considering the significant replacement of indium by manganese in single-phase $CuInSe_2$ samples, we propose that these systems should be investigated for their potential in photovoltaic devices. Additionally, although the doped samples do not show ferromagnetic behavior, a significant tolerance for doping has been demonstrated which still allows these systems to be considered as attractive candidates as parent materials for dilute magnetic semiconductors. It is possible that the compounds can be additionally doped in order to alter their magnetic properties. For example, we have had some preliminary success in simultaneously doping Mn on the indium site and antimony on the selenium site. Other doping possibilities should be considered.

Acknowledgments

This work was supported by the National Science Foundation (NSF) CAREER Award under Grant no. DMR-0645304, and the powder X-ray diffractometer was purchased with funds from the NSF, Grant no. DUE-0511444. C.N.K. thanks NSF-REU, Grant no. CHE-0649182, for support. The authors thank Dr. Cora Lind from the University of Toledo for her useful discussions and Jonathan W. Lekse and Nathan J. Takas of Duquesne University for their helpful experimental assistance.

Appendix A. Supplementary material

Supplementary data associated with this article can be found in the online version at doi:10.1016/j.jssc.2009.07.014.

References

[1] B.J. Stanbery, Crit. Rev. Solid State Mater. Sci. 27 (2002) 73–117.
[2] M.A. Contreras, K. Ramanathan, J. AbuShama, F. Hasoon, D.L. Young, B. Egaas, R. Noufi, Prog. Photovoltaics 13 (2005) 209–216.
[3] S. Schorr, M. Tovar, D. Sheptyakov, L. Keller, G. Geandier, J. Phys. Chem. Solids 66 (2005) 1961–1965.
[4] Y.J. Zhao, A.J. Freeman, J. Magn. Magn. Mater. 246 (2002) 145–150.
[5] Y.J. Zhao, A. Zunger, Phys. Rev. B 69 (2004) 104422.
[6] S.C. Erwin, I. Zutic, Nat. Mater. 3 (2004) 410–414.
[7] T. Dietl, H. Ohno, MRS Bull. 28 (2003) 714–719.
[8] J.K. Furdyna, J. Appl. Phys. 64 (1988) R29–R64.
[9] H. Ohno, J. Magn. Magn. Mater. 200 (1999) 110–129.
[10] G.A. Medvedkin, T. Ishibashi, T. Nishi, K. Hayata, Y. Hasegawa, K. Sato, Jpn. J. Appl. Phys. Part 2 Lett. 39 (2000) L949–L951.
[11] S.L. Cho, S.Y. Choi, G.B. Cha, S.C. Hong, Y. Kim, Y.J. Zhao, A.J. Freeman, J.B. Ketterson, B.J. Kim, Y.C. Kim, B.C. Choi, Phys. Rev. Lett. 88 (2002) 257203.
[12] J.A. Aitken, G.M. Tsoi, L.E. Wenger, S.L. Brock, Chem. Mater. 19 (2007) 5272–5278.
[13] H. Matsushita, M. Watanabe, A. Katsui, J. Phys. Chem. Solids 69 (2008) 294–297.
[14] H. Hahn, G. Frank, W. Klingler, A.D. Meyer, G. Storger, Z. Anorg. Chem. 271 (1953) 153–170.
[15] R. Jenkins, R. Snyder, Introduction to X-ray Powder Diffractometry, Wiley, New York, 1996.
[16] X.p.H. Plus, PANalytical B.V., Almelo, the Netherlands.
[17] A.C. Larson, R.B. Von Dreele, Los Alamos National Laboratory Report LAUR 86 (1994) 748.
[18] B.H. Toby, J. Appl. Crystallogr. 34 (2001) 210–213.
[19] P. Kubelka, F. Munk, Z. Tech. Phys. 12 (1931) 593–601.
[20] S. Stolen, H. Fjellvag, F. Gronvold, J.T. Sipowska, E.F. Westrum, J. Chem. Thermodyn. 28 (1996) 753–766.
[21] N. Elliott, J. Am. Chem. Soc. 59 (1937) 1958–1962.
[22] V.M. Goldschmidt, Norske Vidensk. Akad. Skrifter 1Mat. Naturv. K1 (1927) 1–156.
[23] I.D. Olekseyuk, O.V. Parasyuk, O.A. Dzham, L.V. Piskach, J. Solid State Chem. 179 (2006) 315–322.
[24] G. Zahn, P. Paufler, Cryst. Res. Technol. 23 (1988) 499–507.
[25] J.M. Merino, J.L.M. deVidales, S. Mahanty, R. Diaz, F. Rueda, M. Leon, J. Appl. Phys. 80 (1996) 5610–5616.
[26] W. Paszkowicz, R. Lewandowska, R. Bacewicz, J. Alloy. Compd. 362 (2004) 241–247.
[27] K.S. Knight, Mater. Res. Bull. 27 (1992) 161–167.
[28] L. Kaplan, G. Leitus, V. Lyakhovitskaya, F. Frolow, H. Hallak, A. Kvick, D. Cahen, Adv. Mater. 12 (2000) 366–370.
[29] R.D. Shannon, Acta Crystallogr. A 32 (1976) 751–767.
[30] L. Vegard, H. Dale, Z. Kristallogr. Krist. 67 (1928) 148–161.
[31] Y.J. Zhao, A. Zunger, Phys. Rev. B 69 (2004) 075208.
[32] A. Pietnoczka, R. Bacewicz, S. Schorr, Phys. Status Solidi A Appl. Mater. 203 (2006) 2746–2750.
[33] I. Nakai, M. Izawa, Y. Sugitani, Y. Niwa, K. Nagashima, J. Mineral. 8 (1975) 135–138.
[34] C.I. Pearce, R.A.D. Pattrick, D.J. Vaughan, C.M.B. Henderson, G. van der Laan, Geochim. Cosmochim. Acta 70 (2006) 4635–4642.
[35] V.F. Sears, Neutron News 3 (1992) 26–37.
[36] W. Horig, H. Neumann, H. Sobotta, B. Schumann, G. Kuhn, Thin Solid Films 48 (1978) 67–72.
[37] J.L. Shay, B. Tell, H.M. Kasper, L.M. Schiavone, Phys. Rev. B 7 (1973) 4485–4490.
[38] M.S. Jagadeesh, M.S. Seehra, J. Phys. C Solid State Phys. 15 (1982) 1713–1719.
[39] K.M. Yu, W. Walukiewicz, T. Wojtowicz, I. Kuryliszyn, X. Liu, Y. Sasaki, J.K. Furdyna, Phys. Rev. B 65 (2002) 201303.
[40] J. Blinowski, P. Kacman, Phys. Rev. B 67 (2003) 121204.
[41] Neutron diffraction of undoped and Mn-doped $CuInSe_2$ samples is in progress using the BT-1 neutron powder diffractometer at NIST.